Matter and Radiation at Extremes

RESEARCH ARTICLE | MARCH 20 2024

Radioisotope production using lasers: From basic science to applications

M. R. D. Rodrigues ; A. Bonasera ; M. Scisciò; J. A. Pérez-Hernández; M. Ehret ; F. Filippi; P. L. Andreoli; M. Huault; H. Larreur; D. Singappuli; D. Molloy ; D. Raffestin ; M. Alonzo; G. G. Rapisarda; D. Lattuada ; G. L. Guardo; C. Verona; Fe. Consoli; G. Petringa ; A. McNamee; M. La Cognata; S. Palmerini; T. Carriere; M. Cipriani ; G. Di Giorgio; G. Cristofari; R. De Angelis ; G. A. P. Cirrone; D. Margarone ; L. Giuffrida ; D. Batani ; P. Nicolai ; K. Batani; R. Lera; L. Volpe ; D. Giulietti; S. Agarwal; M. Krupka ; S. Singh; Fa. Consoli

Matter Radiat. Extremes 9, 037203 (2024)
https://doi.org/10.1063/5.0196909

Matter and Radiation at Extremes

RESEARCH ARTICLE

pubs.aip.org/aip/mre

Featured

Radioisotope production using lasers: From basic science to applications

Cite as: Matter Radiat. Extremes 9, 037203 (2024); doi: 10.1063/5.0196909
Submitted: 10 January 2024 • Accepted: 23 February 2024 •
Published Online: 20 March 2024

M. R. D. Rodrigues,[1] A. Bonasera,[1,2,a)] M. Scisciò,[3] J. A. Pérez-Hernández,[4] M. Ehret,[4] F. Filippi,[3] P. L. Andreoli,[3] M. Huault,[5] H. Larreur,[5,6,7] D. Singappuli,[6] D. Molloy,[7,8] D. Raffestin,[6] M. Alonzo,[3] G. G. Rapisarda,[2,9] D. Lattuada,[2,10] G. L. Guardo,[2] C. Verona,[11] Fe. Consoli,[2] G. Petringa,[2] A. McNamee,[8] M. La Cognata,[2] S. Palmerini,[12,13] T. Carriere,[6] M. Cipriani,[3] G. Di Giorgio,[3] G. Cristofari,[3] R. De Angelis,[3] G. A. P. Cirrone,[2] D. Margarone,[8,14] L. Giuffrida,[2,14] D. Batani,[6] P. Nicolai,[6] K. Batani,[15] R. Lera,[4] L. Volpe,[4,16] D. Giulietti,[17] S. Agarwal,[18] M. Krupka,[18,19] S. Singh,[18,19] and Fa. Consoli[3,a)]

AFFILIATIONS

[1]Cyclotron Institute, Texas A&M University, College Station, Texas 77840, USA
[2]Laboratori Nazionali del Sud, Istituto Nazionale di Fisica Nucleare (LNS-INFN), Catania, Italy
[3]ENEA, Fusion and Technologies for Nuclear Safety and Security Department-C, Frascati, Italy
[4]Centro de Láseres Pulsados (CLPU), Villamayor, Spain
[5]Universidad de Salamanca, Salamanca, Spain
[6]Centre Lasers Intenses et Applications (CELIA), Université de Bordeaux, CNRS, CEA, Talence, France
[7]HB11 Energy Holdings Pty, Freshwater, New South Wales, Australia
[8]School of Mathematics and Physics, Queen's University Belfast, Belfast, United Kingdom
[9]Dipartimento di Fisica e Astronomia "E. Majorana," Università di Catania, Catania, Italy
[10]Facoltà di Ingegneria e Architettura, Università degli Studi di Enna "Kore," Enna, Italy
[11]Dipartimento di Ingegneria Industriale, Università di Roma "Tor Vergata," Roma, Italy
[12]Dipartimento di Fisica e Geologia, Università degli Studi di Perugia, Perugia, Italy
[13]Istituto Nazionale di Fisica Nucleare, Sezione di Perugia, Perugia, Italy
[14]ELI Beamlines Facility, The Extreme Light Infrastructure ERIC, Dolni Brezany, Czech Republic
[15]Institute of Plasma Physics and Laser Microfusion (IPPLM), Warsaw, Poland
[16]ETSIA, Universidad Politécnica de Madrid, Madrid, Spain
[17]Dipartimento Fisica, "E. Fermi," Università di Pisa and INFN, Pisa, Italy
[18]FZU–Institute of Physics of Czech Academy of Sciences, Prague, Czech Republic
[19]Institute of Plasma Physics of Czech Academy of Sciences, Prague, Czech Republic

[a)]**Authors to whom correspondence should be addressed:** abonasera@comp.tamu.edu and fabrizio.consoli@enea.it

ABSTRACT

The discovery of chirped pulse amplification has led to great improvements in laser technology, enabling energetic laser beams to be compressed to pulse durations of tens of femtoseconds and focused to a few micrometers. Protons with energies of tens of MeV can be accelerated using, for instance, target normal sheath acceleration and focused on secondary targets. Under such conditions, nuclear reactions can occur, with the production of radioisotopes suitable for medical application. The use of high-repetition lasers to produce such isotopes is competitive with conventional methods mostly based on accelerators. In this paper, we study the production of ^{67}Cu, ^{63}Zn, ^{18}F, and ^{11}C, which are currently used in positron emission tomography and other applications. At the same time, we study the reactions ^{10}B$(p,\alpha)^{7}$Be and ^{70}Zn$(p,4n)^{67}$Ga to put further constraints on the proton distributions at different angles, as well as the reaction ^{11}B$(p,\alpha)^{8}$Be relevant for energy production. The experiment was performed at the 1 PW laser facility at Vega III in Salamanca, Spain. Angular distributions of radioisotopes in the forward (with respect to the laser direction) and backward directions were measured using a high purity germanium detector. Our results are

in reasonable agreement with numerical estimates obtained following the approach of Kimura and Bonasera [Nucl. Instrum. Methods Phys. Res., Sect. A **637**, 164–170 (2011)].

 https://doi.org/10.1063/5.0196909

I. INTRODUCTION

Laser-accelerated proton beams have been applied to radioisotope production for medical purposes by several groups.[1–4] In 2011, Kimura and Bonasera[5] analyzed the feasibility of laser production as an alternative to other methods. Since then, laser technology has greatly improved, and high-repetition lasers in the petawatt regime are available at a cost competitive to accelerator-based systems. These laser systems rely on chirped pulse amplification (CPA)[6] to push laser intensities beyond 10^{18} W/cm^2. At such intensities, ions from the target surface irradiated by the laser beam are accelerated to energies of several MeV by the action of the laser in stripping the less strongly bound electrons from the target and thus creating a strong (repulsive) electric field that accelerates the ions. Without going into the details of the mechanism, we will loosely refer to it as target normal sheath acceleration (TNSA),[1–5] and we discuss an intuitive scenario which we put to an experimental test in this work. We assume that the stripped electrons leave a positively charged target. Ions or protons on the opposite sides of the target surface feel the repulsive Coulomb field, are accelerated, and leave the target area, thus decreasing the Coulomb repulsion. In particular, the shorter the laser pulse, i.e., the faster the laser energy is released on the target, the more rapidly the positive electric field at the target increases. Thus, we may expect higher proton energies for shorter pulses and thin targets.[4] The accelerated ions will move in the direction perpendicular to the target and in *both* directions (i.e., forward and backward) with respect to the laser direction, possibly with different intensities. With protons reaching 60 MeV and above,[7] isotope production becomes possible, and in this context, we will discuss experimental results on the following systems:

(a) ^{63}Cu$(p,n)^{63}$Zn, $Q = -4.15$ MeV;
(b) ^{70}Zn$(p,4n)^{67}$Ga, $Q = -27.68$ MeV;
(c) ^{70}Zn$(p,\alpha)^{67}$Cu, $Q = 2.62$ MeV;
(d) ^{10}B$(p,\alpha)^{7}$Be, $Q = 1.14$ MeV;
(e) ^{11}B$(p,n)^{11}$C, $Q = -2.76$ MeV;
(f) ^{18}O$(p,n)^{18}$F, $Q = -2.44$ MeV.

It is important to note that the reactions above have positive and negative values of Q, and thus from their measurement we will test the proton distribution at different energies.[5] For instance, reaction (b), which has a relatively high threshold energy, requires proton energies above 28 MeV to be produced, whereas reaction (d) with positive Q could occur at any proton energy in principle. We would like to stress that in this work we will concentrate mainly on reactions (a)–(f). Another important study of the present experiment is the reaction ^{11}B$(p,\alpha)^{8}$Be ($Q = 8.7$ MeV) which will be discussed in detail elsewhere.[8]

II. EXPERIMENT AND DATA ANALYSIS

The experiment was performed at the Centro de Láseres Pulsados (CLPU)-VEGA[9] in Salamanca, Spain in November 2022. The laser beam energy was kept near the nominal maximum value of 30 J, while the pulse duration was increased from the lowest possible value of 30–200 fs. A schematic of the scattering chamber is shown in Appendix A. Longer pulses were chosen to try to increase the proton yield at energies around 1 MeV, where the cross section for the fusion reaction ^{11}B$(p,\alpha)^{8}$Be is highest and to improve the shot-to-shot performance stability. The beam was focalized to 6 μm on a 6 μm-thick Al target to produce protons via TNSA (or other mechanisms) from impurities in the target.[4] The facility can deliver one shot per second, but the frequency was limited by the time needed to change the position on the Al target and/or other requirements from the experimental campaign.[8] Many shots were dedicated to determining the energy distributions of protons and other ions, and we took advantage of this possibility to activate different targets located at different angles. While fusion reactions and proton distributions will be discussed in detail elsewhere,[8] here we were interested primarily in nuclear activations to test the theoretical prediction of Ref. 5. A positive comparison with Ref. 5 would confirm that lasers are competitive with other accelerator-based methods to produce radioisotopes for medical, veterinary, and other applications.

Following Refs. 5 and 10, we write the proton distribution function as

$$\frac{d^2N_p}{dEd\Omega} = b(\Omega)\left(\frac{N_1}{\sqrt{\pi E T_1}}e^{-E/T_1} + \frac{N_2}{\sqrt{\pi E T_2}}e^{-E/T_2}\right), \quad (1)$$

where $N_1 = 1.2 \times 10^{13}$, $T_1 = 3.3$ MeV, $N_2 = 2.3 \times 10^{12}$, and $T_2 = 13.5$ MeV are parameters fitted to the experimental results of Ref. 10. Note that Eq. (1) is a phenomenological parametrization of the data, and we are not suggesting that the acceleration is a thermal process. The parameter $b(\Omega)$ is included to reproduce the angular distributions of the reactions. We assume that its integral over solid angle is $\int b(\Omega)d\Omega = 1/5$, where 1/5 is the ratio of the laser energy at Vega III (30 J) to that in Ref. 10 (150 J). There may be a scaling due to the difference in pulse duration,[11] but we will take care of any correction at different angles through $b(\Omega)$. Integrating Eq. (1) over energy and angle under the above assumption gives the total number of protons, say up to 40 MeV maximum energy: $N_p = 2.6 \times 10^{12}$, and decreasing the higher energy limit to 20 MeV gives a difference of less than 1%. Considering a pulse duration of 200 fs, we get a proton current $I_p \sim 10^7$ A, which is an enormous value. If a secondary target is located very close to the Al target, as will be discussed below for some cases, then a plasma may be created by the proton flow. Furthermore, if we accept our naïve picture of the "TNSA mechanism" that electrons are ejected from the Al target in times of the order of the laser pulse duration, then those electrons reach the secondary target before the protons because of the much lighter mass. In this scenario, the secondary target may become negatively charged in a short time, and this may accelerate the positive ions further. The nuclear cross sections and ranges for different reactions may be modified in such an environment, and this could be the

subject of future detailed investigations. Following the same steps as above, we can multiply Eq. (1) by the proton energy and integrate over angle and energy. This gives the total energy provided to the protons $\langle E_p \rangle = 6.7(5.8) \times 10^{12}$ MeV when integrating up to 40 (20) MeV maximum proton energy. This result gives a conversion efficiency from laser energy to proton energy of about 3.1%, assuming that an equal number of protons with the same energy distribution are produced in the back direction. This last assumption will be experimentally tested in this work. The average energy of the protons is $\langle E_p \rangle / N_p = 2.6$ MeV, which would be almost optimal for the 3α fusion reaction. Of course, for reactions having a negative value of Q, the lower limit of integration of the proton distribution is given by $-Q$, and this will cut all the low-energy part of the proton distribution.

We can compare our "benchmark" proton distribution function[10] with other data available in the literature. In Fig. 1, we compare with some selected cases obtained at the SULF laboratory[7] in China using a 2 PW laser focalized to about 6 μm as our case, but at much higher power. The distribution function depends strongly on the detection angle with respect to the Al (or Cu) normal target, decreasing by a factor of more than 3 at 15°. Furthermore, the proton high-energy cutoff decreases when the thickness is increased from 4 to 10 μm. The distribution function from Eq. (1) reproduces rather well the measured one in the region of interest for our work between 5 and 20 MeV. The behavior of the fitted parameter shown in Fig. 1 may be due to the combination of the laser energy and the pulse duration, which are different in Refs. 10 and 11. We expect a similar angular and energy dependence in the back direction as well.

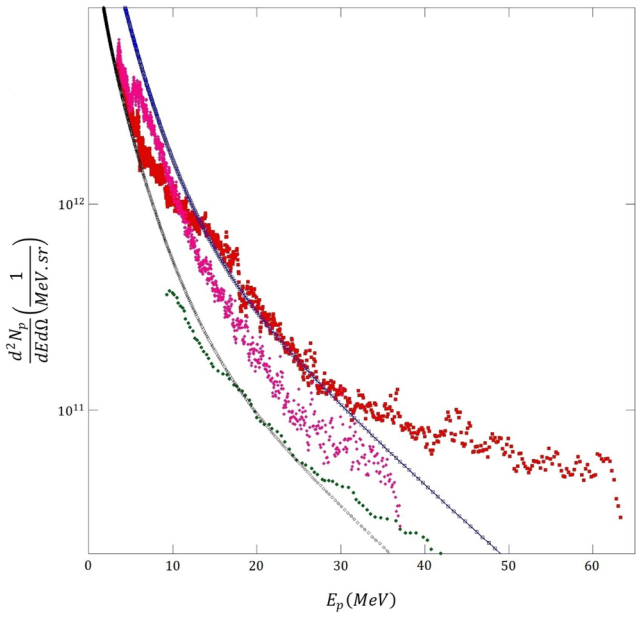

FIG. 1. Proton distribution function (filled symbols) from Ref. 7. The filled (red) squares were obtained at 0° (with respect to the target normal) and the filled (green) circles in the laser direction at 15°. The target thickness was 4 μm. The filled (pink) diamonds were measured at 0°, but for a thickness of 10 μm. Equation (1) was fitted to the 4 μm cases with $b(\Omega) = 15(5)$ sr^{-1}.

A better comparison[8] could be made when the experimental data are measured over different angles and integrated over angles, since the distribution function in Refs. 5 and 10 is integrated over solid angle.

To calculate the number of reactions in the target is a more complicated process, since we need to consider the proton energy distribution, the reaction cross section, and the range of protons in the (assumed cold) target in the limit of a thick target. We can estimate this distribution as

$$\frac{dN}{d\Omega} = \rho \int_{E_{th}}^{E_{max}} \frac{dN_p}{dEd\Omega} \sigma(E) R(E) \left(1 - e^{-d/R(E)}\right) dE, \tag{2}$$

where ρ is the (secondary) target density and d its thickness, $\sigma(E)$ is the reaction cross section of the process (taken from Ref. 12), $R(E)$ is the range obtained from the Stopping and Range of Ions in Matter (SRIM) software,[13] E_{th} is the threshold energy for the reaction to occur (equal to zero for reactions with positive Q). The term in parentheses inside the integral gives the probability that a proton collides with one nucleus of the target. When $d \ll R(E)$, we get

$$\frac{dN}{d\Omega} = \rho d \int_{E_{th}}^{E_{max}} \frac{dN_p}{dEd\Omega} \sigma(E) dE. \tag{3}$$

In the limiting case that the proton distribution is a delta function of the energy (e.g., for accelerators), Eq. (3) reduces to the familiar form used in nuclear physics applications to measure, for instance, the cross section.[14] Following the definition of the astrophysical S-factor, we parameterize the cross sections as

$$\sigma(E) = \frac{S(E)}{E} e^{-b/\sqrt{E}}. \tag{4}$$

$S(E)$ is written in terms of a Taylor expansion in energy;[15] for reactions with negative Q, we write it as

$$S(E) = \sum_i a_i (E + Q)^i, S(E \to -Q) = 0. \tag{5}$$

The free parameters a_i and b are fitted to available experimental data, with the number of parameters being chosen to give good data reproduction. The parameterization in Eqs. (4) and (5) is especially important in energy regions where there are no data.

In Table I, we compare the results of Eq. (2) integrated over angle for different reactions and $E_{\text{max}} = 40$ MeV. These results provide guidance for the present experiment and perhaps for future experiments as well.

There are some important features to notice.

1. The experimental production of ^{67}Ga indicates that there are protons of energy higher than 28 MeV (No. 3 in Table I).
2. If there are enough α-particles produced through the fusion reactions Nos. 5 and 7 in Table I, these could cause other reactions (ternary reactions) when impinging on other targets, for instance, reactions Nos. 10 and 11 in Table I.

In fact, α particles of energy higher than 10 MeV can produce ^{65}Zn, and this would indicate that their energy distribution is modified[16] by high-energy protons.[8] Thus, measurement of the distribution function of α particles is crucial, and for this purpose, Columbia Resin #39 (CR39), a solid-state nuclear track detector, is mostly used, since other methods are not effective owing to the large

TABLE I. Expected reaction rates N (corrected by concentration) using Eq. (2) and assuming $\int b(\Omega)d\Omega = 1/5$. The E_γ column refers to the highest intensity γ ray emitted by the isotope; $T_{1/2}$ is the half-life.[12]

No.	Reaction	Target	Thickness (mm)	N (10^8)	Q (MeV)	E_γ (keV)	$T_{1/2}$
1	^{63}Cu(p,n)^{63}Zn	^{nat}Cu	1	1.4	−4.15	511	38.5 min
2	^{63}Cu(p,n)^{63}Zn	^{63}Cu	0.011	0.11	−4.15	511	38.5 min
3	^{70}Zn(p,4n)^{67}Ga	^{70}Zn	0.032	1.8×10^{-3}	−27.68	93.3	3.26 d
4	^{70}Zn(p,α)^{67}Cu	^{70}Zn	0.032	2.6×10^{-3}	2.62	185	2.57 d
5	^{10}B(p,α)^{7}Be	^{nat}B	2	0.28	1.15	477.6	53.2 d
6	^{11}B(p,n)^{11}C	^{nat}B	2	1.4	−2.76	511	20.4 min
7	^{11}B(p,α)^{8}Be	^{nat}B	2	2.2	8.6	⋯	8 10^{-17} s
8	^{12}C (p,X)^{11}C	CR39	1	0.1	−16.5	511	20.4 min
9	^{12}C(p,p)3α	CR39	1	0.88	−7.27	⋯	⋯
10	^{63}Cu(α,X)^{65}Zn	^{nat}Cu	1	⋯	−10.4	1115.5	244 d
11	^{65}Cu(α,X)^{68}Ga	^{nat}Cu	1	⋯	−5.8	511	67.7 min
12	^{18}O(p,n)^{18}F	^{nat}B (^{18}O 8.7 × 10^{-5}%)	2	3	−2.44	511	109.7 min

number of protons and other particles produced in the plasma.[8,16–19] For this reason, we have estimated possible reactions occurring in the CR39 detector (which is rich in C ions) giving the same products coming from the main reactions such as 3α (No. 9) and ^{11}C (No. 8). As we can see from Table I, those reactions are quite competitive, especially if high-energy protons are produced through the "TNSA mechanism." It is important to stress that reactions with negative Q are often competitive with those with positive Q. This is strictly dependent on the proton energy distribution (which can reach high values), the corresponding cross section, and the range. In the following subsections, we will discuss in detail the main experimental findings and compare them with Table I.

A. ^{63}Cu(p,n)^{63}Zn, ^{63}Cu(α,X)^{65}Zn, and ^{65}Cu(α,X)^{68}Ga

Thin ^{63}Cu targets were mounted on CR39 both for support and to measure the energy distribution of the incident protons (and other ions if possible) that went through the target (see Fig. 2). The targets were located at different angles and distance with respect to the Al target. Note that if high-energy protons collide with the CR39, ^{11}C may be produced (reaction No. 8 in Table I), and this γ-decays with energy 511 keV, the same as the decay of ^{63}Zn. In such cases, the half-lives can be determined (or other signature γs) when it is possible to distinguish the two cases.

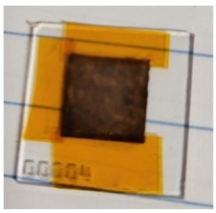

FIG. 2. Photograph and properties of the ^{63}Cu target used in the experiment. The target is mounted on CR39 (acting as a support and proton detector) with pieces of Kapton tape.

It is also important to determine the number of reactions produced per shot, since we were in the multi-shot accumulation regime. Even in the case of large fluctuations from shot to shot,[8] it is possible to define an average over many shots, N_{av}. The produced isotopes decay with decay constant λ, and thus we give a weight to each shot according to $\Pi = e^{-\lambda(t_0 - t_{shot})}$ and sum over all shots. Here, t_0 is the starting measurement time using the high purity germanium (HPGe) detector and t_{shot} is the time when the shot occurred (see Fig. 3), and for more details, see Appendix B.

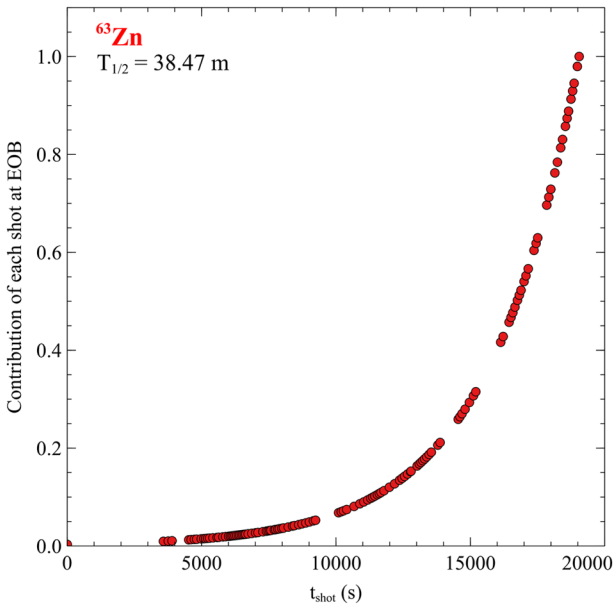

FIG. 3. Probability contribution of each shot to the reaction ^{63}Cu(p,n)^{63}Zn at end of bombardment (EOB) as a function of shooting time starting from the first shot (t_{shot} = 0 s) to the last, when the chamber was opened and the sample decays were measured using the HPGe detector. The well-known half-life $T_{1/2}$ of ^{63}Zn was used to produce this result.

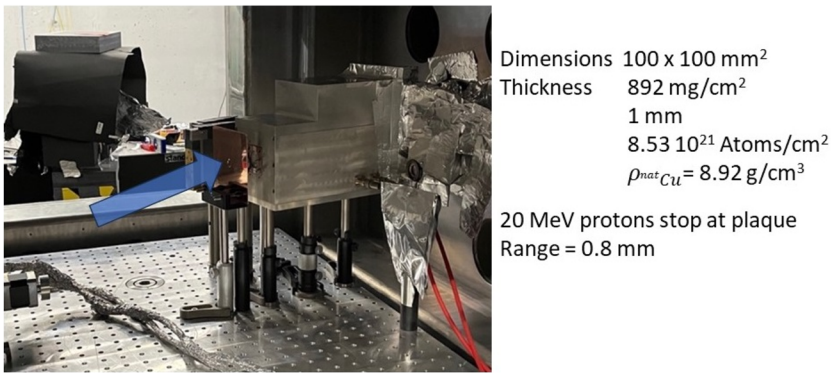

FIG. 4. The ^{nat}Cu target mounted in front of the Thomson parabola spectrometer. Note the hole at the center of the target to let the energetic ions into the spectrometer. This position defines our 0° where the largest number of protons, indicated in the figure by the arrow, is found. A diagram of the experiment can be found in Appendix A.

In Table I, reactions Nos. 1 and 2, it is clearly demonstrated that for thin targets, the produced yield is very small (and comparable to the reaction rates obtained for CR39), and therefore we repeated the analysis using a thick target of ^{nat}Cu at different angles; see Fig. 4 for the case at 0°, where the largest number of produced protons occurs. We expect an increase in yield of at least an order of magnitude (Table I), and the higher statistics allow us a more detailed analysis.

In Fig. 5, we show the background-subtracted β-delayed γ -ray spectrum using the thick ^{nat}Cu target located at 0° with respect to the Al target perpendicular direction. At this angle (see Fig. 4), we expect the proton TNSA yield to be the highest. The full-energy-peak (FEP) at 511 keV is more intensely populated, a signature of ^{63}Zn being produced (see Table I, reaction No. 1). Furthermore, other FEPs associated with lower-intensity ^{63}Zn decays are clearly observed.

In Fig. 6, we plot the counting rate vs time for the 0° case, where the statistics are large enough. We clearly see that the decay is in perfect agreement with the well-known half-life of ^{63}Zn, demonstrating that there are no other competing reactions (e.g., reactions with the ^{65}Cu in the target).

Standard analysis techniques were applied to derive the number of produced isotopes at the end of irradiation (see, e.g., Refs. 20–23). The final experimental uncertainties are simple propagations of the peak statistics, detector efficiencies, and fit uncertainties. The corrections due to the detector dead time, the backscattering peak, and the respective summed coincidences, source self-absorption, and isotopic enrichment, were also considered in the results; see Appendix B for more details.

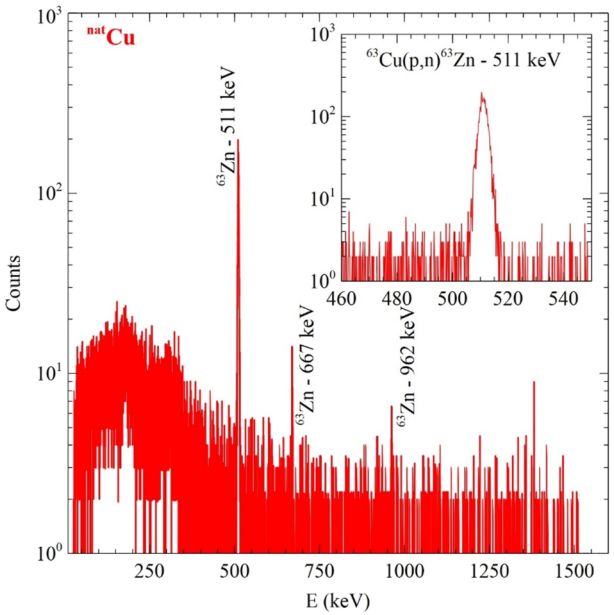

FIG. 5. Background-subtracted β-delayed γ-ray spectrum using the thick ^{nat}Cu target. The main contribution for the FEP at 511 keV, magnified in the inset, comes from the ^{63}Zn decay produced in the ^{63}Cu(p,n)^{63}Zn reaction. Other lower-intensity γs associated with the ^{63}Zn decay are also visible.

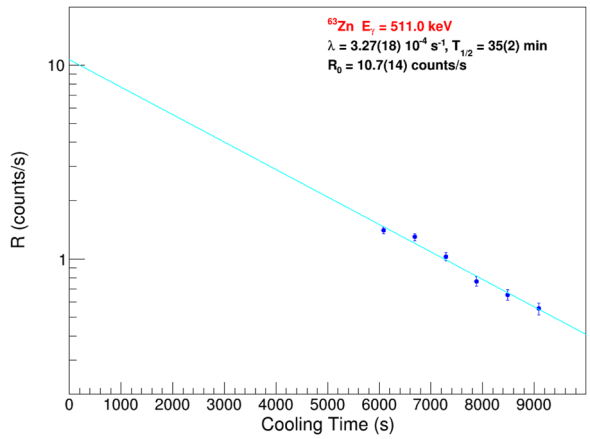

FIG. 6. Counting rate decay as a function of cooling time. The fitted decay constant λ and the associated half-life $T_{1/2}$ displayed here confirm that the decaying nucleus is ^{63}Zn. The fitted half-life $T_{1/2}$ is presented on the figure.

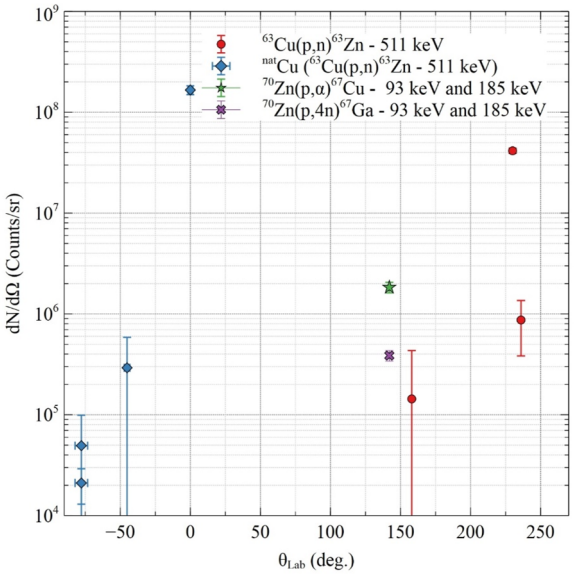

FIG. 7. Summary of yields at different angles obtained using the targets indicated in the inset. Angles between −90° and +90° are in the forward direction, and from 90° to 270° are in the back direction of the Al target, producing protons through the "TNSA mechanism" (see Appendix A).

In Fig. 7, we plot the results for the Cu targets as filled circles and diamonds. The ^{nat}Cu gives a peak at 0° as expected, whereas the thin ^{63}Cu exhibits its largest value at 230°. For the latter case, we would expect a maximum at 180°, but we could not install a target at such an angle because of obstructing optics. In any case, these results clearly demonstrate that the proton yield in the back direction is as strong as that in the forward direction. Since the distribution is so strongly peaked, we cannot estimate the total yield integrated over the forward direction, because we measured too few angles. However, as we will show in Sec. II C, we can estimate the opening angle of the produced protons in the forward direction[7,8,19] and obtain $\Delta\Omega = 0.59 \pm 0.18$ sr. This gives an average number of produced ions per shot $N(^{63}\mathrm{Zn}) \approx (dN/d\Omega)\Delta\Omega = (1.1 \pm 0.3) \times 10^8$ in fair agreement with the estimate in Table I. Shooting at 1 Hz for 2 h at Vega III, we may get 345 ± 94 MBq. Alternatively, one could use a laser with a lower energy but a higher repetition rate. For instance, Vega II in Salamanca, Spain delivers 6 J in 30 fs at 10 Hz (see also Ref. 19). If we assume the same laser energy scaling as for Table I, this laser will produce twice as much radioisotope as the estimate above, but at a much lower cost. A major problem in this approach may be connected to the time to align the "TNSA target" of choice at high frequency.

From reaction No. 2 in Table I, we would expect the result at 230° to be one order of magnitude smaller with respect to the 0° result because of the different target thicknesses. Since the ^{63}Cu target was mounted on (thick) CR39 (see Fig. 2), we cannot exclude the contribution from ^{11}C decays from reaction No. 8 in Table I, if protons with energies above 16.5 MeV are produced at such angles. Unfortunately, for this case, the statistics were poor and did not allow us to do a time evolution study as in Fig. 6. Other γs produced in the decay of ^{63}Zn are comparable to the background, at variance with the results of Fig. 5. Another reason could be that more protons are produced in the back direction,[19] thus giving a higher yield than predicted. A detailed angular and energy distribution of the protons is not the goal of this work and will be discussed elsewhere.[8] The use of CR39 as a support for our thin targets will provide important constraints on the proton distribution for these angles. Furthermore, the choice of using a stack of two CR39s, not clearly visible in Fig. 2, will allow unambiguous measurement of high-energy protons (if any) that went through the first CR39 and stopped in the second one.[8]

It should be noted that we have two results at −90° using the ^{nat}Cu target. For these two separate series of shots, a ^{nat}B target was installed in front of the Al target in the catcher–pitcher (CP) configuration.[8] Since the B target is rather thick, we expect the produced α particles to remain trapped, except those produced at the surface and emitted in the back direction.[8] Thus, we installed the ^{nat}Cu at −90° to capture the α particles and activate it through (but not only) reactions Nos. 10 and 11 in Table I. As we see from Fig. 7 and as expected, at such angles, the proton distribution should be depleted, and thus a signal coming from the α particles may be detectable. Reactions Nos. 5–7 in Table I may occur in such a configuration. The experimental γ spectra for such cases do not show any activations that can be attributed to the α particles. Even from this negative result we may learn something: we could increase the probability of α reactions by locating the Cu target closer to the B target, thus increasing the solid angle. A better option is to use the CP configuration, but with a mixture of B and another element that can be unambiguously activated by the α particles. In such a case, an experimental constraint on the α distribution may be obtained.[20]

As shown in Fig. 4, the ^{nat}Cu target was conveniently located in front of the Thomson parabola (TP) spectrometer.[8,9] Proton energy distributions for each shot were recorded, and their average value and fluctuations from shot to shot are displayed in Fig. 8, as

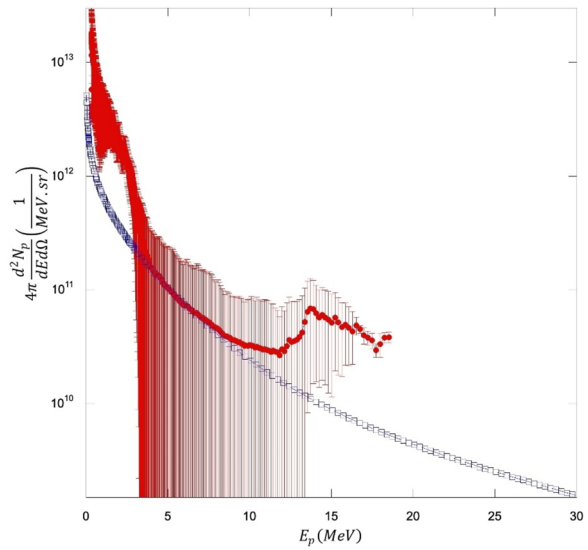

FIG. 8. Proton distribution measured at 0° (filled red circles) with the TP detector. The large error bars are fluctuations from shot to shot due to different experimental conditions.[8] The data are normalized to Eq. (1) (open blue squares) with $4\pi b(0) = 1.5 \pm 0.3$ sr^{-1}.

Dimensions 7 x 10 mm^2
Thickness 22.8 mg/cm^2
32 μm
1.96 10^{20} Atoms/cm^2
$\rho_{^{70}Zn}$= 7.14 g/cm^3

20 MeV protons Energy Loss = 351 keV

FIG. 9. The ^{70}Zn target mounted on the CR39 and installed at 130° (back direction); see also Fig. 7.

compared with Fig. 1. The TP is not calibrated, and thus we have normalized the data to our adopted proton distribution in the region of 5–10 MeV where most of the ^{63}Zn yield is produced according to our calculations using Eqs. (1)–(5). The parameter in Eq. (1), $4\pi b$ (0) = 1.5 ± 0.3 sr^{-1}, was fixed to reproduce the yield obtained with the ^{nat}Cu target at 0°. This may serve as a preliminary calibration, but the important point is that protons close to 20 MeV are observed, and we cannot exclude the possibility that even higher-energy protons are also produced, but their yield is below the sensitivity of the TP[8] (see Fig. 8).

B. ^{70}Zn(p,α)^{67}Cu and ^{70}Zn(p,4n)^{67}Ga

Reactions Nos. 3 and 4 in Table I, apart from being interesting for medical applications,[20,22,24] may provide some further constraint on the proton distribution (in the back direction) because of the different Q value. In particular, to produce ^{67}Ga, protons with energies higher than 28 MeV are needed, and we did not observe any with the TP located in the front direction (see Fig. 8). However, the proton distribution in the back direction can be quite different from that in the front direction.[20]

In Fig. 9, we show the ^{70}Zn target used in our experiment. As in the ^{63}Cu case, the CR39 was added for support and to measure the proton distribution;[8] however the support was removed when measuring the γ yield using the HPGe detector. To estimate the yields for reactions Nos. 3 and 4 in Table I, the cross sections are needed. The ^{67}Cu case has been rather well studied and the cross section is well known, whereas data are scarce for the ^{67}Ga case. As we discussed above, we parameterized the cross sections using Eqs. (4) and (5). For the ^{67}Ga case, some data are available, but at high proton energies.[25] We used four fitting parameters to reproduce the proton energy threshold value and the data at high energies.

In Fig. 10, we compare our parametrization with the data from Ref. 25. To the best of our knowledge, no data are available in the region near 30 MeV that makes the highest contribution to the yield reported in Table I. Furthermore, the fact that the yields of the two reactions are comparable (for proton energies higher than 30 MeV) can be attributed to the greater than one order of magnitude difference in the cross sections, especially at high energies (see also Figs. 3 and 6 in Ref. 25). In particular, the reaction cross section to produce ^{67}Cu reaches at most 20 mb, whereas for ^{67}Ga, a cross section of about 300 mb was measured.[25]

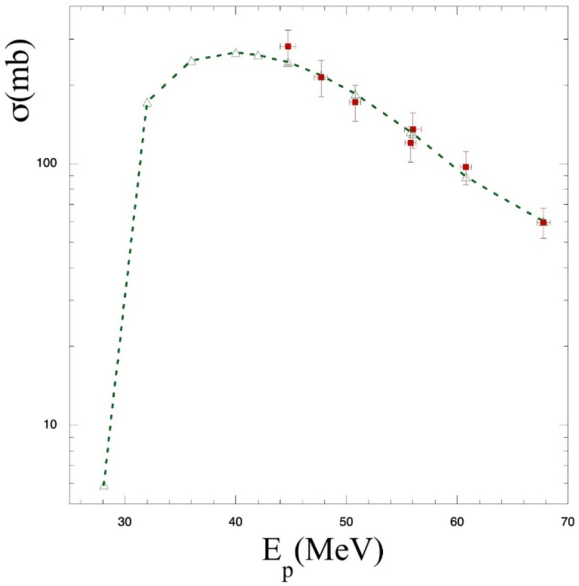

FIG. 10. Cross section for the reaction ^{70}Zn(p,4n)^{67}Ga as a function of proton energy. The data (filled squares) are taken from Ref. 25. The parametrization using Eqs. (4) and (5) is given by the open triangles joined by the dashed line.

The two peaks corresponding to the decays of ^{67}Ga and ^{67}Cu at 91–93 and 185 keV are clearly visible in Fig. 11; see also the inset in the figure for the region of interest. Note that the lower-energy peak (91–93 keV) is more intense than that at 185 keV. The γ intensities per 100 decays of the β-decay parent for ^{67}Cu are I_γ(%) = 13.2 and 48.7 for the two energies,[12] and thus we would expect the 185 keV peak to be more intense. On the other hand, for ^{67}Ga, I_γ(%) = 42.4 and 21.2, respectively[12] (see Table I). Using the well-known intensities for the two nuclei, we can solve a simple set of two equations with two unknowns to obtain their respective yields. The values obtained are plotted in Fig. 7 as star and cross symbols. They are much smaller than those in the ^{63}Zn case, as expected from Table I, but higher than our estimates, which may suggest that the proton yield in the back direction is higher than that in the front.[19] This is consistent with the high yield seen for the ^{63}Cu case at 230°.

C. ^{11}B(p,n)^{11}C

In Table I, we have estimated the total yield for the reaction No. 6 in good agreement with Ref. 5. In the spirit of the catcher–pitcher configuration,[8] we placed a thick natural boron target at a few centimeters from the "TNSA" Al target. The B target was slightly tilted with respect to the normal direction to "focus" some α particles produced at the surface to −90°, where we installed the ^{nat}Cu target, another TP, and CR39[8] (see Appendix A). Many shots were performed on each target, and γ decays from the ^{nat}B target were measured with the HPGe detector. The ^{11}C yields for different measurements are reported in Fig. 12, together with pictures of the B targets after irradiation. The slightly ellipsoidal proton spots on the targets can be clearly seen, and we can measure their sizes. For instance, the spots for targets "5 November" to "18 November" give

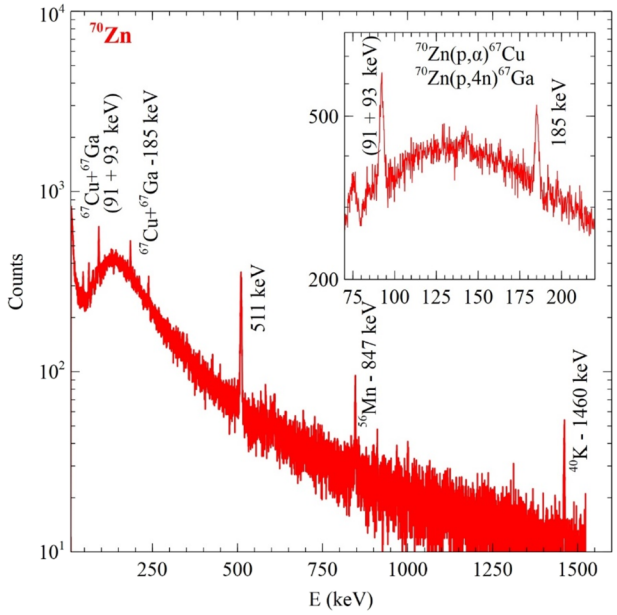

FIG. 11. The β-delayed γ-ray spectrum for a ^{70}Zn target. The FEPs at 91–93 keV (within the energy resolution of the HPGe detector) and at 185 keV contain the contributions from the decay of ^{67}Cu and ^{67}Ga produced in the ^{70}Zn(p,α)^{67}Cu and ^{70}Zn(p,4n)^{67}Ga reactions. This spectrum was measured with the original acquisition system (see Appendix B) and is not background-subtracted. The FEP count rates for 511 and 1460 keV are 0.012 and 0.0014 counts/s, respectively, which are compatible with the background measured with the new acquisition system. We have also identified a peak corresponding to ^{56}Mn, probably coming from activation of some impurities. Another possibility is given by the reaction ^{70}Zn(p,^{56}Mn)^{15}C; $Q = -15.2$ MeV, $T_{1/2} = 2.6$ h.

an area of the order of 1 cm^2. The distance from the Al target is well known, and this gives the proton opening angle $\Delta\Omega = 0.59 \pm 0.18$ sr that we have already used in Sec. II A. Since all the produced protons are collected by the ^{nat}B, the measured ^{11}C rate is the total yield in the front direction. As we can see from Fig. 12, the measured yield is very close to our estimate in Table I[5] and could be probably improved a little. Note that for the first two cases in Fig. 12, the yield was a factor of 2 less than our estimate, because a little space was left between the two ^{nat}B targets to let protons get through and be measured with a TP and/or diamond detectors.[8]

The targets used had a 99.6% concentration of ^{nat}B (80% ^{11}B, 20% ^{10}B), with the remaining contaminants being mainly N, O, and H. In Refs. 20 and 26, the possibility was discussed that produced α particles may interact with N impurities and produce ^{18}F, i.e., ternary collisions may occur.[12,18] The latter decays with the production of 511 keV γ rays just like ^{11}C, but with a different lifetime. ^{13}N and ^{18}F can be produced by protons colliding with target "impurities" (^{14}N or ^{18}O).[20] Those elements have a very small concentration in the target (but much higher than the α produced through reactions Nos. 5 and 7 in Table I), and we expect a negligible contribution, but one in competition with ternary collisions.

In Fig. 13, we plot the 511 keV γ counting rate for the B target in the pitcher–catcher configuration. A fit to the experimental curve with free fitting of half-lives and assuming three components gives a

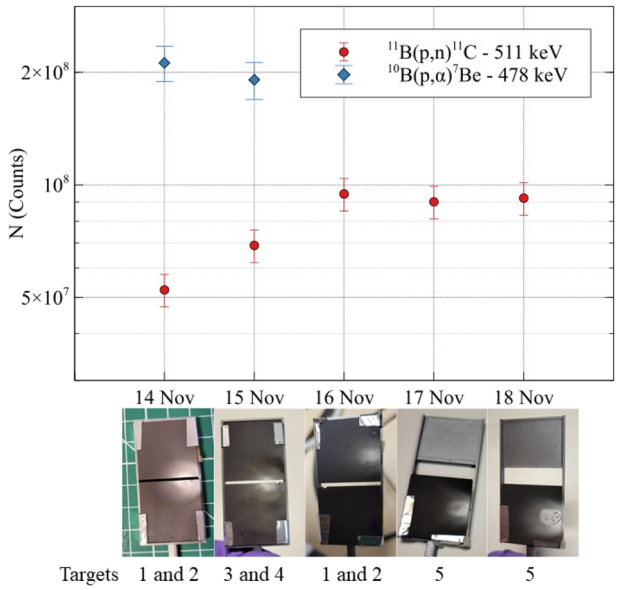

FIG. 12. ^{11}C (filled circles) and ^{7}Be (filled diamonds) yields produced in the collisions of TNSA protons with the ^{nat}B targets shown below the plot as they were at the end of each measurement. The proton spot size is clearly visible, and its opening angle can be estimated as discussed in the text. All results have been corrected for the ^{11}B–^{10}B concentrations.

100% contribution from the decay of ^{11}C. To obtain an upper limit on the production of the two other isotopes, we fixed their half-lives and reran the fit. This gave a zero contribution from ^{13}N, which is not surprising, since its half-life is shorter than that of ^{11}C, and thus its contribution is relevant only at short times when ^{11}C is dominant. ^{18}F has a longer half-life, and its presence can be seen from the decay

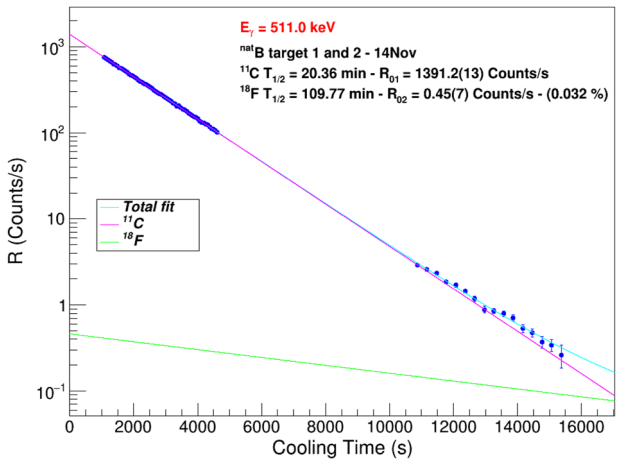

FIG. 13. Counting rate for 511 keV γ rays emitted from the B target as a function of time. The fixed half-lives $T_{1/2}$ are indicated. The rate can be fitted with just the ^{11}C decay. To put an upper limit for other ions, we have forced the fit using the half-lives of ^{11}C and ^{18}F. The data support less than 0.032% ^{18}F production for targets 1 and 2 in Fig. 12.

rate at longer times. In Fig. 13, we show the result of a fit in which the half-lives of ^{11}C and ^{18}F were fixed. This gives an upper limit of 0.032% on the contribution of ^{18}F, as in Ref. 20, which is compatible with the low ^{18}O concentration and thus excludes any ternary collisions, as expected.[18,20,27] This result was obtained with the configuration indicated as targets 1 and 2 in Fig. 12, i.e., a configuration where the two B targets are slightly displaced. In this case, a certain number of protons propagated *in vacuo* and were detected by the TP at 0°. If we repeat the same analysis for ^{18}F, but with the B target completely blocking the proton flow (targets 3–5 in Fig. 12), the production of ^{18}F increases to 0.15%. This difference may be simply understood by inspecting Eq. (2) and realizing that all the terms are the same for the two cases, apart from the number of protons, which must be decreased.

D. ^{10}B(p,α)^{7}Be

In the ^{nat}B target, we can also produce ^{7}Be from reaction No. 5 in Table I.[17] Its half-life is much longer than those in the previous cases, which means that the shot contribution at different times has practically weight 1 as shown in Fig. 14 (compare this with Fig. 3).

The γ spectrum for these reactions is dominated by ^{11}C at shorter times, whereas at longer times, only ^{7}Be remains. Furthermore, the γ energy decay of ^{7}Be (478 keV) is quite different from that of ^{11}C (511 keV) and can be quite easily distinguished in the plot (see Fig. 15).

The produced yield of ^{7}Be is displayed in Fig. 12 and is in fair agreement with our estimate for reaction No. 5 in Table I, after correction by the concentration. Since we had just one HPGe detector available, the two first cases only were measured for a long time to allow an unambiguous determination of ^{7}Be.

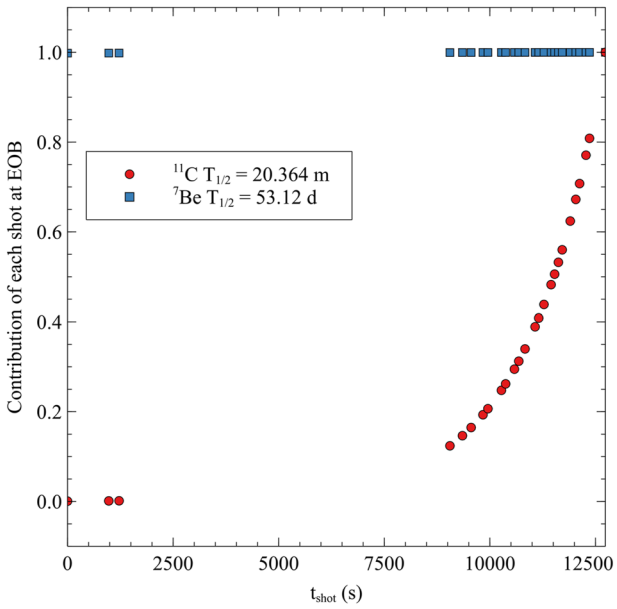

FIG. 14. Probability contribution of each shot to the production of ^{11}C and ^{7}Be isotopes at end of bombardment (EOB) as a function of shooting time starting from the first shot (t_{shot} = 0 s) to the last shot when the chamber was opened and the sample decays were measured using the HPGe detector. The well-known half-lives $T_{1/2}$ of both isotopes were used to produce this result.

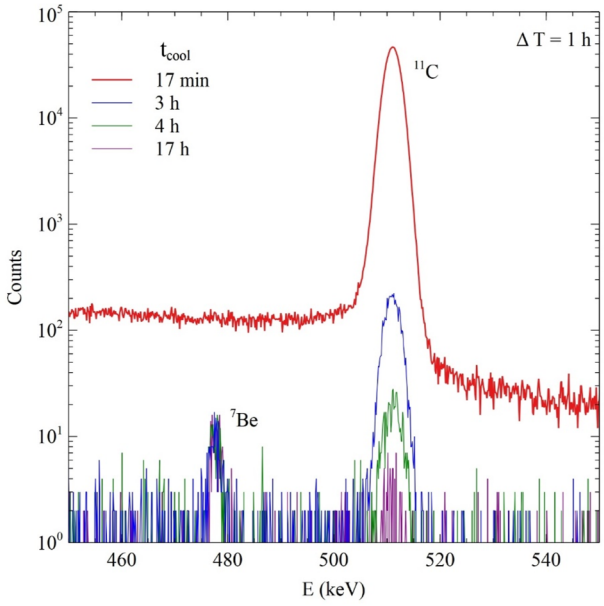

FIG. 15. Region of interest for the background-subtracted β-delayed γ-ray spectrum for the ^{nat}B targets 1 and 2 exposed on 14 November at four different cooling times t_{cool} for a measurement time of ΔT = 1 h. For the shortest cooling time, the ^{11}C decays dominate, whereas ^{7}Be becomes dominant at longer cooling times.

III. CONCLUSIONS

We have investigated nuclear reaction products using the PW laser at Vega III in Salamanca, Spain. The pitcher–catcher method was adopted, with protons produced by an aluminum target and impinging on several different targets, both in the forward and the back direction with respect to the laser direction. We found the production of medical radioisotopes to be in agreement with expectations and the predictions of Ref. 5, thus supporting its conclusions. Laser technology is now sufficiently mature for it to compete with accelerators for radioisotope production. Their relative competitiveness may be determined by construction costs, space available, maintenance requirements, and other factors, but from our experience, we predict that lasers may turn out to be the winners here.

Of course, cyclotrons do have the advantage that their beam energy can be adjusted to produce particular radionuclides, whereas with lasers, a wide energy spectrum of protons is generated, at least when they are produced by the TNSA mechanism.[28–31] This may lead to many additional reactions taking place inside the irradiated target [e.g., (p,n) and (p,2n)], which may result in reduced radionuclide purity and specific activity of the produced nuclides. However, this can be easily corrected using a degrader if the proton energies are too high, thereby reducing the number of undesired products, or by using magnetic fields to select a narrower energy spectrum from the obtained proton beam. The real advantage of cyclotrons, however, is their ability to accelerate more complex ions (d, α, and even heavy nuclei in inverse kinematics[21–24]) for production. Acceleration

of heavier nuclei using lasers, on the other hand, is still a formidable task that will require future investigation.

We have also estimated theoretically the production of different nuclei and made some assumptions regarding the cross sections in energy regions where they have not been measured. The "TNSA mechanism" should be studied in in detail and adjusted to account for the various physical scenarios that one would like to implement. In particular, the role of electrons must be clarified and, if possible, used to favor nuclear reactions in the plasma. This may be crucial if we are to apply this method to neutron-less reaction energy production. Our predictions in Table I have been rather well confirmed by the data we have obtained. In particular, the reaction $^{11}B(p,\alpha)^{8}Be$ will be discussed in more detail elsewhere.[8] The values obtained here are too small for self-sustained reactions to occur, and we may need to compress the catcher.[18,27]

ACKNOWLEDGMENTS

We wish to express out particular thanks to all the personnel at the CLPU–Vega facility for their direct and indirect help. We thank Mr. A. Massara (LNS-INFN, Catania-Italy) for providing to specification the thin targets used in the experiment. We thank Dr. B. Roeder for the digital acquisition support. We thank Mr. Zhe-Zhu for pointing out some misprints and a careful check of the results in Table I.

This work was supported in part by the United States Department of Energy under Grant No. DEFG02-93ER40773; the EUROfusion Consortium, funded by the European Union via the Euratom Research and Training Program (Grant Agreement No. 101052200—EUROfusion); and the COST Action Grant No. CA21128—Proton Boron Nuclear Fusion: From Energy Production to Medical Applications (PROBOBO), supported by COST (European Cooperation in Science and Technology—www.cost.eu).

AUTHOR DECLARATIONS

Conflict of Interest

The authors have no conflicts to disclose.

Author Contributions

A.B. devised the scheme to measure radioisotopes and wrote the first draft of the paper. M.R.D.R. performed the data analysis for the HPGe detector and M.E. the data analysis for the zero-degree TP. F.C. was the spokesperson of the main experiment for α production. All authors contributed to the experimental proposal and preparation and on the final form of the manuscript.

M. R. D. Rodrigues: Conceptualization (equal); Formal analysis (equal); Methodology (equal); Software (equal); Writing – review & editing (equal). **A. Bonasera**: Conceptualization (equal); Data curation (equal); Formal analysis (equal); Funding acquisition (equal); Supervision (equal); Validation (equal); Writing – original draft (equal). **M. Scisciò**: Data curation (equal); Investigation (equal); Writing – review & editing (equal). **J. A. Pérez-Hernández**: Data curation (equal); Investigation (equal); Writing – review & editing (equal). **M. Ehret**: Data curation (equal); Investigation (equal); Writing – review & editing (equal). **F. Filippi**: Data curation (equal); Investigation (equal); Writing – review & editing (equal). **P. L. Andreoli**: Data curation (equal); Investigation (equal); Writing – review & editing (equal). **M. Huault**: Data curation (equal); Investigation (equal); Writing – review & editing (equal). **H. Larreur**: Data curation (equal); Investigation (equal); Writing – review & editing (equal). **D. Singappuli**: Data curation (equal); Investigation (equal); Writing – review & editing (equal). **D. Molloy**: Data curation (equal); Investigation (equal); Writing – review & editing (equal). **D. Raffestin**: Data curation (equal); Investigation (equal); Writing – review & editing (equal). **M. Alonzo**: Data curation (equal); Investigation (equal); Writing – review & editing (equal). **G. G. Rapisarda**: Data curation (equal); Investigation (equal); Writing – review & editing (equal). **D. Lattuada**: Data curation (equal); Investigation (equal); Writing – review & editing (equal). **G. L. Guardo**: Data curation (equal); Investigation (equal); Writing – review & editing (equal). **C. Verona**: Methodology (equal); Resources (equal); Writing – review & editing (equal). **Fe. Consoli**: Data curation

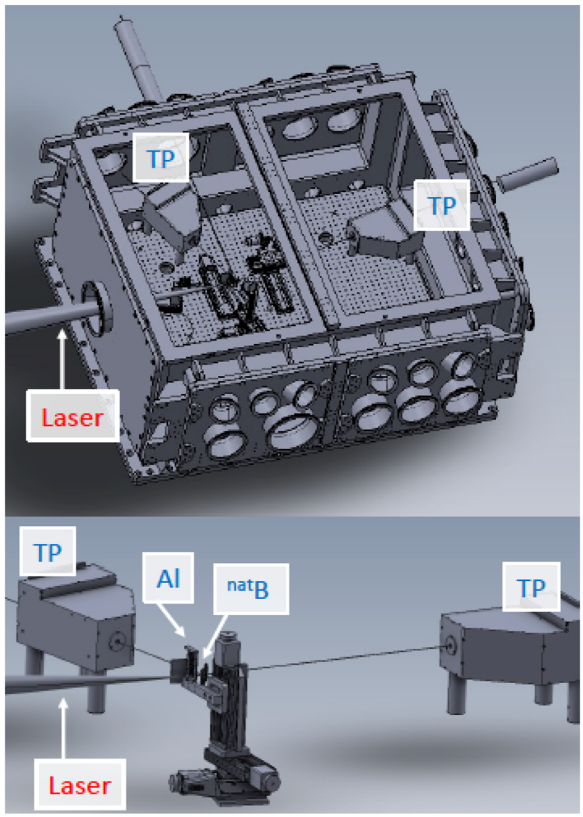

FIG. 16. Schematic of the scattering chamber. In the top panel, the laser is impinging from the left on the Al target (to produce protons). The Al target is slightly tilted with respect to the laser direction to avoid dangerous reflections. The protons move in the direction perpendicular to the Al target and are detected by the forward TP, which defines 0°, while the second TP is located at −90°. In the bottom panel, the ^{nat}B is in front of the Al to collect the protons produced in the forward direction. In this pitcher–catcher configuration, the TP at 0° is (partially) obstructed.

(equal); Investigation (equal); Writing – review & editing (equal). **G. Petringa**: Data curation (equal); Investigation (equal); Validation (equal); Writing – review & editing (equal). **A. McNamee**: Data curation (equal); Investigation (equal); Writing – review & editing (equal). **M. La Cognata**: Data curation (equal); Investigation (equal); Writing – review & editing (equal). **S. Palmerini**: Data curation (equal); Investigation (equal); Writing – review & editing (equal). **T. Carriere**: Formal analysis (equal); Methodology (equal); Software (equal); Writing – review & editing (equal). **M. Cipriani**: Investigation (equal); Methodology (equal); Project administration (equal); Supervision (equal); Validation (equal); Writing – review & editing (equal). **G. Di Giorgio**: Data curation (equal); Investigation (equal); Writing – review & editing (equal). **G. Cristofari**: Data curation (equal); Investigation (equal); Writing – review & editing (equal). **R. De Angelis**: Conceptualization (equal); Validation (equal); Writing – review & editing (equal). **G. A. P. Cirrone**: Conceptualization (equal); Formal analysis (equal); Supervision (equal); Writing – review & editing (equal). **D. Margarone**: Conceptualization (equal); Supervision (equal); Validation (equal); Writing – review & editing (equal). **L. Giuffrida**: Conceptualization (equal); Investigation (equal); Methodology (equal); Writing – review & editing (equal). **D. Batani**: Conceptualization (equal); Supervision (equal); Writing – review & editing (equal). **P. Nicolai**: Formal analysis (equal); Methodology (equal); Software (equal); Writing – review & editing (equal). **K. Batani**: Data curation (equal); Investigation (equal); Writing – review & editing (equal). **R. Lera**: Data curation (equal); Investigation (equal); Methodology (equal); Writing – review & editing (equal). **L. Volpe**: Data curation (equal); Funding acquisition (equal); Methodology (equal); Project administration (equal); Supervision (equal); Writing – review & editing (equal). **D. Giulietti**: Data curation (equal); Visualization (equal); Writing – review & editing (equal). **S. Agarwal**: Data curation (equal); Investigation (equal); Writing – review & editing (equal). **M. Krupka**: Data curation (equal); Investigation (equal); Methodology (equal); Writing – review & editing (equal). **S. Singh**: Data curation (equal); Investigation (equal); Methodology (equal); Writing – review & editing (equal). **Fa. Consoli**: Conceptualization (equal); Funding acquisition (equal); Project administration (equal); Supervision (equal); Validation (equal); Writing – review & editing (equal).

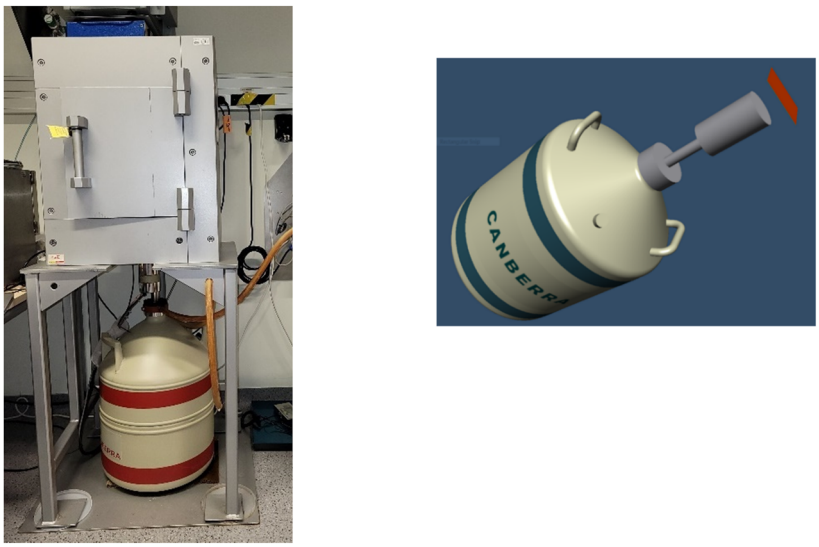

FIG. 17. (a) Photographs of the HPGe detector and its passive iron shielding. (b) Plot generated by LabSOCS for a plaque source of 100 × 100 mm^2 at 110 mm from the detector cap, together with the corresponding efficiency curve. The efficiency curves for source plaques of 10 × 10 mm^2 and 25 × 50 mm^2 are also shown for comparison.

DATA AVAILABILITY

The data that support the findings of this study are available from the corresponding author upon reasonable request.

APPENDIX A: EXPERIMENTAL SET UP

Figure 16 shows a schematic of the scattering chamber.

APPENDIX B: GAMMA SPECTROSCOPIC ANALYSIS

1. Detector properties and calibration

A Canberra XtRa Model GX3019[32] high-purity germanium (HPGe) detector was used for the γ-spectroscopic analysis. This is a coaxial germanium detector with a thin-window contact on the front surface and with a passive iron shield of 15 cm in all directions [see Fig. 17(a)]. The original acquisition system consisted of a DSA-1000, a 16 k multichannel analyzer (MCA) using digital signal processing techniques, paired with GENIE 2000, a comprehensive environment for data acquisition, display, and analysis of γ spectrometry.[32] This system was used just for the measurements of the ^{70}Zn target. For all the other measurements, another updated acquisition system was used, based on a CAEN DT5781 quadruple independent 16 k digital MCA and CoMPASS, a multiparametric data acquisition software for physics applications.[33] The main advantage of this setup is the capability to have a timestamp for each event, as well as the availability of an updated computer system.

The HPGe detector dead time was 1%–10% and the energy resolution 1.0–2.5 keV (FWHM). The distances from the detector cap to the sources were in the range of 20–120 mm. The 20 mm distance was used only for sources with low activities. The γ-ray spectra were measured and analyzed up to 1600 keV. Measurements of the ^{22}Na, ^{155}Eu, and ^{137}Cs sources were performed at different cap-to-source distances on different days. These measurements were used in the calibration of the detector energy and efficiency. The absolute photopeak efficiencies for the different source–detector distances and source geometries were determined using the results on the experimental efficiencies from the source measurements and LabSOCS mathematical efficiency calibration software.[32] Efficiency curves generated by LabSOCS for plaque sources of 10 × 10 mm^2, 25 × 50 mm^2, and 100 × 100 mm^2 are presented in Fig. 17(b) as illustrative examples. The room background was measured during the experiment and subtracted in the analysis.

2. Spectrum and time evolution analysis

The data consist of the energy and timestamp for each event. An example of an energy vs timestamp histogram is shown in Fig. 18(a). Depending on the half-life of each radionuclide of interest, spectra for different intervals of time ΔT are generated. Figure 18(b) presents spectra generated for ΔT = 60 s to analyze the time evolution of ^{11}C ($T_{1/2}$ = 20.36 min). The room background spectrum is normalized to ΔT and subtracted from each generated spectrum. The net areas of the full energy peaks (FEPs) are obtained through a Gaussian and background fit considering the Compton scattering background. In cases where the statistics are too low and the Gaussian fit is not adequate to determine the area, the net area is obtained from the integral of the raw spectra at a fixed width and the integral of the room background spectrum normalized to ΔT at the same width is subtracted.

The next step is the fit of the FEP rate as a function of time to identify the contributions of possible radionuclides with half-lives that are sufficiently different to allow separation in the fit (see Figs. 6 and 13). A full spectrum analysis is also performed to determine any possible coproduced radionuclides with similar half-lives. Once the identification has been made, the number of radionuclides measured is determined using the respective FEP rate:

$$N_{\mathrm{exp}} = \frac{R}{\lambda \varepsilon_{\mathrm{HPGe}} I_\gamma}, \tag{B1}$$

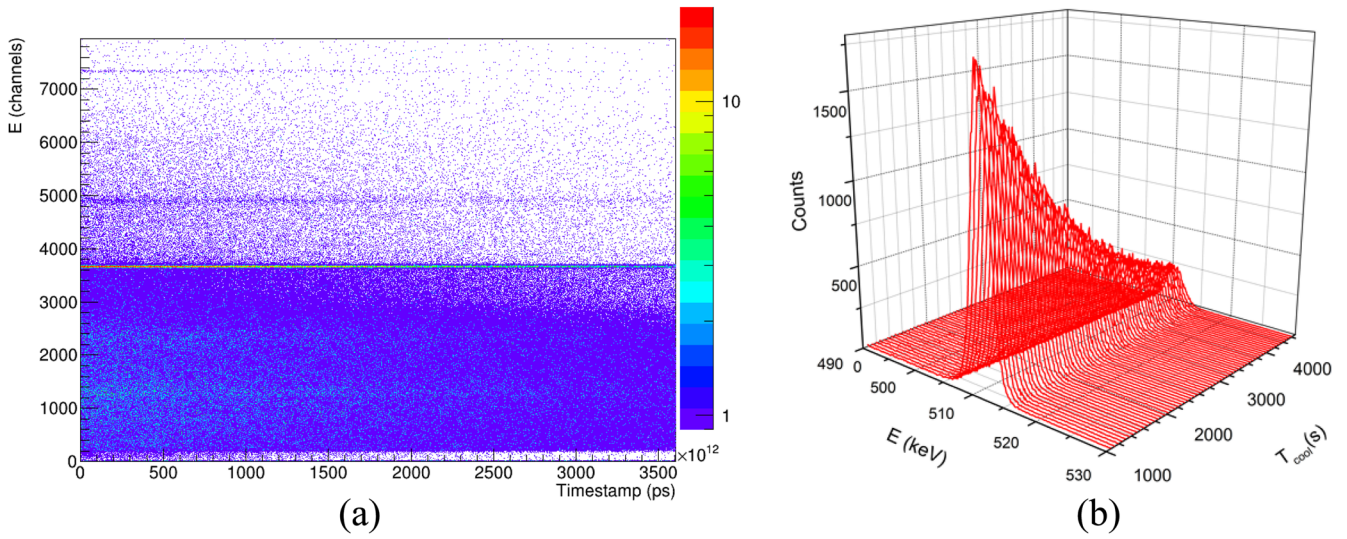

FIG. 18. (a) Energy vs timestamp raw data and (b) corresponding spectra generated using 60 s time intervals for ^{11}C analysis. The line at E(channels) = 3671 corresponds to the FEP at energy E_γ = 511 keV.

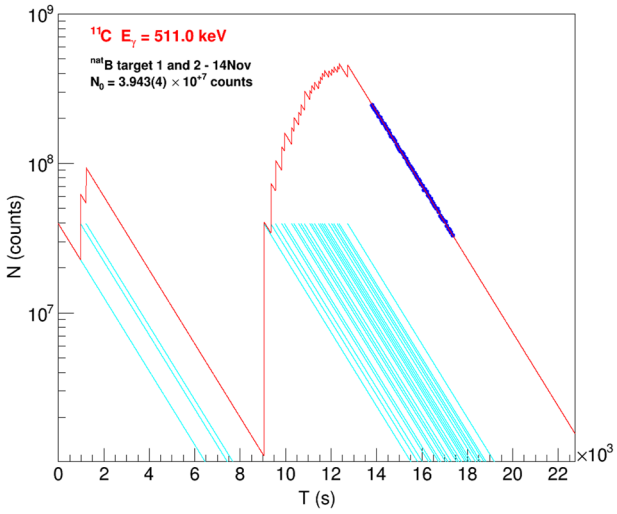

FIG. 19. Number of radionuclides produced as a function of time. The first laser shot is at $T = 0$ s. The blue points are the numbers of radionuclides obtained from the γ-spectroscopic analysis [Eq. (B1)], and the solid red line represents a fit of Eq. (B2) to experimental data. Jumps in the plot correspond to the times at which a laser shot occurred. The cyan lines represent the contributions for each shot.

where R is the photo-peak rate at energy E_γ, $\varepsilon_{\mathrm{HPGe}}$ is the detector efficiency of the HPGe detector at the γ energy considered, I_γ is the intensity of the γ line of interest, and λ is the decay constant of the radionuclide. Considering production and decay in a multi-shot accumulation regime, the number of radionuclei produced is given by

$$N(t) = \sum_{i=0}^{n} N_{0i} e^{-\lambda(t-t_{\mathrm{shot}i})} \approx N_0 \sum_{i=0}^{n} e^{-\lambda(t-t_{\mathrm{shot}i})} \qquad \text{(B2)}$$

for $t > t_{\mathrm{shot}n}$, where $t = 0$ s is the time of the first shot and $t_{\mathrm{shot}i}$ the time of the subsequent shots, n is the number of shots, and N_{0i} is the number of particles produced at shot i. If the average number of particles produced at each shot is assumed to be N_0, then the approximation on right-hand side of Eq. (B2) can be used to fit the N_{exp} data and obtain the value of N_0, as shown on Fig. 19.

The corrections due to backscattering and coincidence summing peaks for ^{11}C (0.17%–0.35%), γ self-absorption up to 4%, and the isotopic enrichment of the respective targets were also included in the results. The uncertainties are propagation of the net area of the FEPs and the detector efficiency uncertainties. The lower limit of detection was identified as 0.015(3) particles/s.

REFERENCES

[1] I. Spencer *et al.*, "Laser generation of proton beams for the production of short-lived positron emitting radioisotopes," Nucl. Instrum. Methods Phys. Res., Sect. B **183**, 449 (2001).
[2] K. W. D. Ledingham *et al.*, "High power laser production of short-lived isotopes for positron emission tomography," J. Phys. D: Appl. Phys. **37**, 2341 (2004).
[3] E. Amato *et al.*, "Future laser-accelerated proton beams at ELI-Beamlines as potential source of positron emitters for PET," J. Instrum. **11**, C04007 (2016).
[4] A. Macchi, M. Borghesi, and M. Passoni, "Ion acceleration by superintense laser-plasma interaction," Rev. Mod. Phys. **85**, 751 (2013).
[5] S. Kimura and A. Bonasera, "Deuteron-induced reactions generated by intense lasers for PET isotope production," Nucl. Instrum. Methods Phys. Res., Sect. A **637**, 164–170 (2011).
[6] D. Strickland and G. Mourou, "Compression of amplified chirped optical pulses," Opt. Commun. **56**, 219 (1985).
[7] A. X. Li *et al.*, "Acceleration of 60 MeV proton beams in the commissioning experiment of the SULF-10 PW laser," High Power Laser Sci. Eng. **10**, e26 (2022).
[8] F. Consoli *et al.*, "Laser-Initiated ^{11}B(p,α)2α fusion reactions in petawatt-scale, high repetition rate laser facilities" (unpublished).
[9] See https://www.clpu.es for information about high-repetition-rate petawatt laser VEGA III at CLPU (Centro de Láseres Pulsados), the Spanish Center for Pulsed Lasers.
[10] D. S. Hey *et al.*, "Laser-accelerated proton conversion efficiency thickness scaling," Phys. Plasmas **16**, 123108 (2009).
[11] S. Kimura and A. Bonasera, "Hydrodynamic scaling analysis of nuclear fusion driven by ultra-intense laser-plasma interactions," Int. J. Mod. Phys. E **21**(12), 1250102 (2012).
[12] See https://www.nndc.bnl.gov for National Nuclear Data Center (NNDC), Brookhaven National Laboratory.
[13] See http://www.srim.org for the Stopping and Range of Ions in Matter Software, Srim, J. Ziegler.
[14] D. Lattuada *et al.*, "Model-independent determination of the astrophysical S factor in laser-induced fusion plasmas," Phys. Rev. C **93**, 045808 (2016).
[15] C. Angulo *et al.*, "A compilation of charged-particle induced thermonuclear reaction rates," Nucl. Phys. A **656**, 3 (1999).
[16] S. Kimura *et al.*, "Comment on 'Observation of neutronless fusion reactions in picosecond laser plasmas,'" Phys. Rev. E **79**, 038401 (2009).
[17] A. Bonasera *et al.*, "*Measuring the astrophysical S-factor in plasmas*," in *4th International Conference on Fission Properties of Neutron Rich Nuclei* (World Scientific, Sanibel Island, 2007), p. 541.
[18] M. Huang, H. J. Quevedo, G. Zhang, and A. Bonasera, "Nuclear astrophysics with lasers," Nucl. Phys. News **29**(3), 9–13 (2019).
[19] D. Giulietti *et al.*, Nucl. Instrum. Methods Phys. Res., Sect. B **402**, 373 (2017).
[20] M. S. Schollmeier, "Investigation of proton beam-driven fusion reactions generated by an ultra-short petawatt-scale laser pulse," Laser Part. Beams **2022**, 2404263.
[21] G. A. Souliotis *et al.*, "A novel approach to medical radioisotope production using inverse kinematics: A successful production test of the theranostic radionuclide ^{67}Cu," Appl. Radiat. Isot. **149**, 89–95 (2019).
[22] M. R. Dias Rodrigues *et al.*, "Production of ^{99}Mo in inverse kinematics heavy ion reactions," Radiat. Phys. Chem. **212**, 111162 (2023).
[23] M. R. Dias Rodrigues *et al.*, "A novel approach to medical radioisotope production using inverse kinematics," EPJ Web Conf. **252**, 08002 (2021).
[24] J. Mabiala *et al.*, "Enhanced production of ^{99}Mo in inverse kinematics heavy ion reactions," EPJ Web Conf. **252**, 08003 (2021).
[25] G. Pupillo *et al.*, "Production of ^{67}Cu by enriched ^{70}Zn targets: First measurements of formation cross sections of ^{67}Cu, ^{64}Cu, ^{67}Ga, ^{66}Ga, ^{69m}Zn and ^{65}Zn in interactions of ^{70}Zn with protons above 45 MeV," Radiochim. Acta **108**(8), 593–602 (2020).
[26] C. Labaune, C. Baccou, V. Yahia, C. Neuville, and J. Rafelski, "Laser-initiated primary and secondary nuclear reactions in boron-nitride," Sci. Rep. **6**(1), 21202 (2016).
[27] G. Zhang *et al.*, "Nuclear probes of an out-of-equilibrium plasma at the highest compression," Phys. Lett. A **383**, 2285 (2019).
[28] C. Perego, D. Batani, A. Zani, and M. Passoni, "Target normal sheath acceleration analytical modeling, comparative study and developments," Rev. Sci. Instrum. **83**, 02B502 (2012).
[29] M. Passoni, C. Perego, A. Sgattoni, and D. Batani, "Advances in target normal sheath acceleration theory," Phys. Plasmas **20**, 060701 (2013).
[30] D. Batani, G. Boutoux, F. Burgy, K. Jakubowska, and J. E. Ducret, "Proton acceleration measurements using fs laser irradiation of foils in the target normal sheath acceleration regime," Phys. Plasmas **25**, 054506 (2018).

[31] V. Malka, J. Faure, S. Fritzler, M. Manclossi, A. Guemnie-Tafo, E. d'Humières, E. Lefebvre, and D. Batani, "Production of energetic proton beams with lasers," Rev. Sci. Instrum. **67**, 03B302 (2006).

[32] See https://mirion.com for Mirion Technologies Products for Gamma Spectroscopy.

[33] See https://caen.it for the eletronic instrumetation CAEN company.